

Montanuniversität Leoben

Influence of Fe impurities
on structure and properties of AlCrN films
grown by cathodic arc evaporation

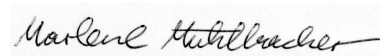


This work has been carried out at the Chair of Functional Materials and Materials Systems at the Department of Physical Metallurgy and Materials Testing, Montanuniversität Leoben, Austria in collaboration with the Christian Doppler Laboratory for Advanced Hard Coatings.

Affidavit

I declare in lieu of oath, that I wrote this thesis and performed the associated research myself, using only literature cited in this volume.

Leoben, November 23, 2011

A handwritten signature in black ink, reading "Marlene Hubilacker", is written on a light-colored rectangular background.

Acknowledgement

I would like to express my sincere gratitude to Univ.-Prof. Christian Mitterer for providing me with the opportunity of writing this thesis at his chair with the thin film group, where I have learned so much over the last years.

A huge Thank You! is due to Robert. I couldn't have wished for a better advisor! Always patient and good humored, he kept me from stumbling on the long and winding paths of research and scientific writing, and, best of all, he is also a fan of British English.

I am also very grateful to Claudia, who first introduced me to the beauty of thin films and hard coatings.

Many thanks go to all the members of the thin film group, especially to Stephan, who acquainted me with L^AT_EX; Marisa, who helped with the first depositions; Rosti, the guru of nanoindentation; Oliver for all the troubles he took with the DSC; Nina, who supplied me with alumina crucibles; and Hannes and Veli for moral support during Mutti-measurements. Special thanks are due to Prof. Paul Mayrhofer and his PhD-group for fruitful discussions regarding the TGA measurements.

I am grateful to Mrs Hilde Stopar and Ms Regina Kranz for helping with all bureaucratic problems and to Mrs Silvia Pölzl as well as DI Christopher Pöhl for demonstrations in metallography and DSC/TGA, respectively.

I would also like to take this opportunity to thank all my friends for keeping me company throughout my years in Leoben, especially: "Meine Mädels" Astrid, July, Marion and Tamara, who are now scattered over the whole wide world: I miss the endless talks, the lunch breaks and the chocolate fondues! Manu aka "The High Priestess of the Kitchen", who put up with all my peculiarities, though she didn't always appreciate my music. And Marco, who appreciates all kinds of music, for the great time we had (and have) together.

Last but not least I would like to thank my parents: My Dad for the financial support and countless taxi services to and from the train station, and my Mum for looking after my pets when I was not at home (especially for walking the dog at 5 am and calling the fire brigade when the cat was stuck on the chimney).

An honorary mention goes to Penny and the sisters from the subterranean world, who are the best.

Contents

1	Theoretical Aspects	1
1.1	The Arc Evaporation Process	1
1.2	Thin Film Structure	3
1.2.1	Fundamental Structure Forming Phenomena	3
1.2.2	Structure Zone Models	5
1.3	Fundamentals of the AlCrN-System	6
1.3.1	Crystal Structure and Properties	6
1.3.2	The Influence of Alloying Elements	8
1.4	Target Fabrication	9
	Bibliography	11
2	Manuscript	13
3	Outlook	30

1 Theoretical Aspects

1.1 The Arc Evaporation Process

Arc evaporation belongs to the area of physical vapour deposition (*PVD*) techniques. It was first utilised technically in the eighteenth century by J. Priestly, who successfully deposited brass and silver on a glass substrate using a primitive capacitor as an energy source. Over the next 250 years arc evaporation emerged as an industrial process due to increasing understanding of the physical principles involved and the considerable improvements in vacuum technology [1].

The arc evaporation process is unique among other deposition techniques. Material is evaporated by an arc discharge between two electrodes, where the target material typically forms the cathode. Hence, the process is also often referred to as *cathodic arc evaporation*. The arc discharge occurs at low voltages ranging from 20-100 V and high currents between 30 A and several kA. A non-stationary local spot of high current density (in the order of 10^{12} Am⁻²) is formed on the cathode surface. This area of a few square micrometres is called *cathode spot*. Cathode spots move randomly over the cathode surface and are centres of strong particle and electron emission. Interactions between such electrons and the target vapour atoms lead to the formation of a self-sustaining highly ionised (up to 100%) plasma [2-4].

Spot ignition often takes place at surface asperities on the cathode, where the electric field is concentrated. This leads to extreme heating of the asperity. The material at the cathode spot region transforms from the solid state via the liquid and vapour phase to a plasma. After the initial explosion and ionisation, the plasma expands away from the cathode spot. Ignition and explosion typically occur in a time range of 1-10 ns with the lifetime of the cathode spot being of the order of 100 ns. The plasma density near the cathode spot reaches values of 10^{26} m⁻³ but drops significantly as the plasma expands. The ions present in the plasma can reach charge states of 3, 4, and above, especially in the case of refractory metals as target materials. All ions have a high velocity of approximately 10^4 ms⁻¹, which corresponds to a kinetic energy of about 20 eV

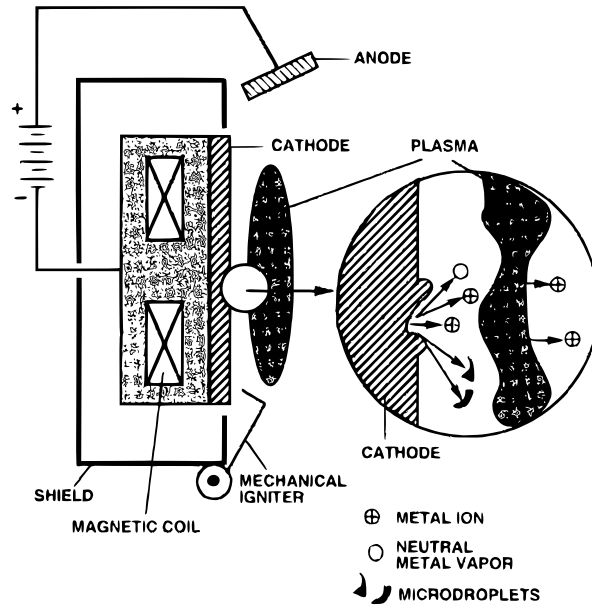


Fig. 1.1: Schematic of a cathodic arc source with the detail on processes at the cathode spot [6].

for light elements and 200 eV for heavy elements. These high ion energies and the substantial degree of plasma ionisation are the main features of the arc evaporation process [1, 2]. They allow for good control over the film morphology at relatively low substrate temperatures. Film properties such as density and adhesion can be enhanced. Additionally, arc evaporation permits the conservation of alloy composition from the target material to the growing film, but most films are deposited from metallic targets in a reactive atmosphere [5], which is also the case for the films deposited within this work.

A major drawback of arc evaporation, however, is the emission of debris particles and droplets from the cathode spot. If material is heated sufficiently to melt but not to sublime, particles in the range of 0.01-10 μm are emitted during plasma explosion. They can be incorporated into the growing film, where they cause the formation of voids or even large scale defects in the film structure. As a consequence, the performance of hard coatings and functional films may be affected negatively [1, 2]. The most promising approach to completely remove debris particles and droplets seems to be magnetic filtering of the plasma prior to deposition [3].

The typical arrangement of a cathodic arc source used in deposition systems is depicted in Fig. 1.1. It consists of the electrodes, a power supply and control circuit, a cooling system (not shown) and an igniter. Ignition of the arc can be achieved by a

mechanical trigger or an electrical discharge. To avoid erosion of other materials at cathode potential, the arc spot itself must be confined to the cathode surface. If a passive border confinement is used, the erosion of the cathode will be uniform [5]. However, a more common alternative is magnetic steering of the cathode spot. It allows for a better control of the spot motion and reduces macroparticle emission. Typically, the erosion pattern is circular and referred to as *racetrack* [1].

Cathodic arcs can be operated in pulsed or continuous mode, whereas the deposition rates are higher in the latter. Hence, most arc systems in industrial applications operate in direct current mode. This permits large area, high-throughput deposition [3].

1.2 Thin Film Structure

1.2.1 Fundamental Structure Forming Phenomena

Film formation occurs if a sufficient number of vapour particles (viz. atoms and ions) condense and adsorb on the substrate surface. These *ad-particles* may diffuse until they reach energetically advantageous surface sites. Due to interactions with other ad-particles the assembly of metastable clusters proceeds. According to the thermodynamic principles of nucleation, clusters will only become stable if they exceed a critical size. A comparison of the three basic growth modes that can be distinguished at this stage [6, 7] is shown in Fig. 1.2. *3-D island* or *Volmer-Weber growth* typically predominates for deposition of metal and semiconductor films on oxide substrates. The bond strength of the deposited particles between each other is significantly higher than to the substrate. Soon after initial nucleation, numerous uniformly distributed and highly mobile clusters or islands of condensed vapour particles are observed on the substrate surface. Further impinging particles and smaller clusters are incorporated. Hence, the average island size increases whereas the island density saturates. The subsequent merging of the islands is termed *coalescence*. The coalesced cluster generally adopts the crystallographic orientation of the initially larger island, since the driving force is the minimisation of surface and interface energy. Coalescence leads to the development of a connected network with unfilled channels. With further deposition the channels eventually fill in completely and the film is said to be continuous. These processes account for the first few hundred Ångstroms of film thickness.

If the particles are more strongly bound to the substrate than to each other, the nucleus will grow in two dimensions which results in the formation of planar monolayers. This

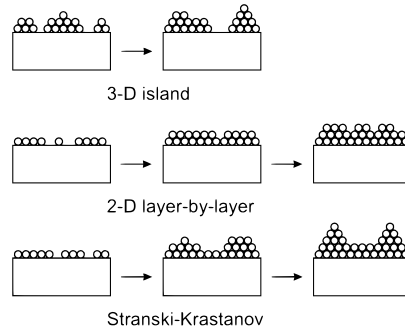


Fig. 1.2: Comparison of the basic modes of thin film growth [6].

regime is called *2-D layer-by-layer* or *Frank-Van der Merwe growth* and is characteristic for single-crystal epitaxial growth of semiconductor films. A combination of the previous two modes is *Stranski-Krastanov growth*, where the layer structure becomes energetically unfavourable after initial formation and island growth commences. This regime is fairly common in metal-metal and metal-semiconductor systems.

Apart from the film and substrate material, film formation is also influenced by the flux and kinetic energy of the impinging particles and the growth temperature as well as the surface cleanliness, crystallinity, and orientation [6, 7]. In cathodic arc evaporation technology (Sect. 1.1) it is also possible to apply a bias potential to the substrate. This has a strong influence on particle interactions and enhances film adhesion. As a further benefit, deposition of compounds can be achieved at relatively low substrate temperatures (100-400 °C), because of the additional activation energy obtained from the bias potential and the plasma [5].

Adsorption and incorporation of impurities may inhibit (decrease in grain size) or promote (increase in grain size) the fundamental structure forming phenomena. Inhibitors form two dimensional covering layers on growing crystal surfaces and grain boundaries. Thus, crystal shapes become rounded and truncated, which leads to dome-shaped surface features in continuous films. If the impurities cover the complete surface, secondary nucleation sets in and the resulting films are two phase systems. Impurity phases also inhibit grain boundary migration causing a further decrease in grain size and a weak texture or even random orientation. A promotion of structure formation and increasing grain size was observed for Al films under co-deposition of Sn and In. Moreover, these additives also reduced the inhibition effect of oxygen on the structure evolution of Al thin films [8].

1.2.2 Structure Zone Models

Considering the temperature dependence of structure evolution in polycrystalline thin films, various structure zone models have been developed. Barna and Adamik [8] present a compilation of structure zone models which have been published so far. It is reprinted in Fig. 1.3. Four distinct structure zones are discernible with increasing homologous temperature (ratio of substrate temperature and melting temperature of the coating material).

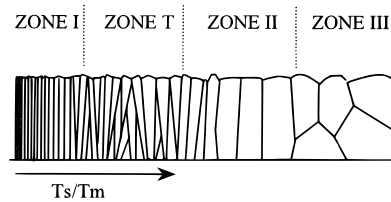


Fig. 1.3: Main characteristics of structure zones with increasing homologous temperature as used in literature [8].

In *zone I* (temperature interval $0 < T_s/T_m < 0.2$), the fibrous structure is homogeneous and determined by nucleation density and statistical fluctuation. The diameter of the fibers increases with increasing T_s/T_m from about 1 to 10 nm. Defect density is high in the crystals and the grain boundaries are porous. In this temperature range neither bulk nor surface diffusion is noteworthy.

Zone T (temperature interval $0.2 < T_s/T_m < 0.4$) represents a transition and develops by competitive growth of differently oriented crystals. Therefore, it consists of fine fibers near the substrate which merge into V-shaped grains with rising film thickness and can even become columnar in thick films. Surface diffusion is pronounced while grain boundary migration is limited.

In *zone II* ($T_s/T_m > 0.4$) the film is homogeneously composed of columns virtually perpendicular to the film plane. Strong restructurisation, such as coalescence and grain coarsening, occurs because of the elevated grain boundary mobility.

Bulk and interface diffusion dominate at high substrate temperatures in *zone III*. This leads to the formation of recrystallised globular grains. However, the development of this kind of structure can also be attributed to the presence of inhibiting impurity species and may exist at every substrate temperature [6, 8].

Barna and Adamik [8] have introduced the concept of *real structure zone models*, taking into account the segregation of active impurity species and the formation of surface covering layers. The influence of increasing impurity concentration on film structure is

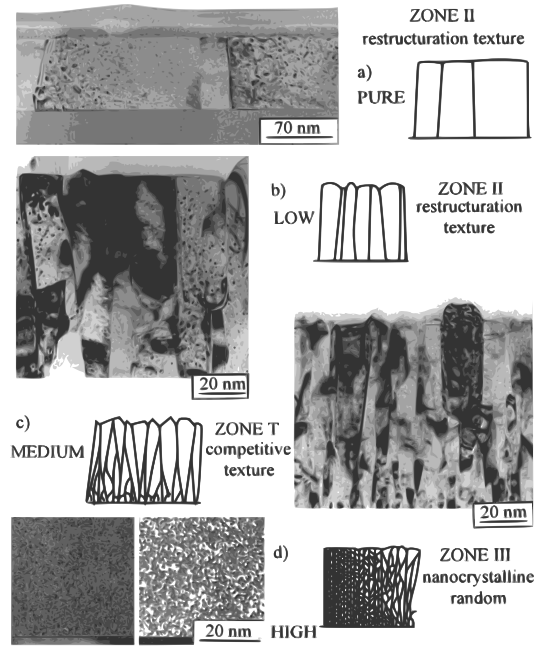


Fig. 1.4: Structural characteristics of Al thin films deposited by thermal evaporation at room temperature and standard high vacuum conditions (a), at low (b), medium (c), and high (d) levels of oxygen contamination [8].

shown in Fig. 1.4 for an aluminium/oxygen system. Deposition was performed at room temperature. This corresponds to zone II in the basic structure zone model as described above. At low levels of oxygen contamination (Fig. 1.4b) the film will retain a columnar structure. Nonetheless the columns will be smaller than those in a pure Al film (Fig. 1.4a) due to the inhibited mobility of grain boundaries. If the oxygen content is increased (Fig. 1.4c), competitive growth (as in zone T) related to the segregation properties of oxygen on the different crystal planes will begin. At high oxygen concentrations (Fig. 1.4d) nano-sized globular grains with random orientation according to zone III will be formed because the developing oxygen surface layer impedes grain growth.

In general, the control of these processes allows for the specific tailoring of thin film structures (eg. nanocrystalline or extremely large crystalline) [8].

1.3 Fundamentals of the AlCrN-System

1.3.1 Crystal Structure and Properties

AlCrN has been established as a protective hard coating due to its excellent wear resistance and thermal stability. Even though the binary nitrides CrN and AlN have a

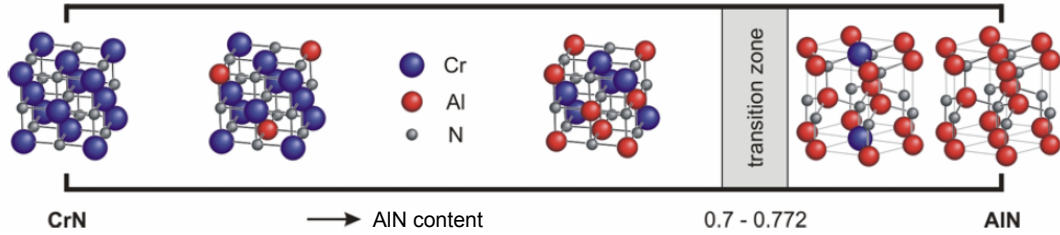


Fig. 1.5: Crystal structures of AlCrN films. A transition from the fcc to the hcp configuration occurs at AlN contents of 0.700-0.772 [4, 10].

low solubility for each other, PVD techniques allow for the synthesis of metastable solid solutions of $\text{Al}_x\text{Cr}_{1-x}\text{N}$ because of the high cooling rates. The resulting structure is dependent on the chemical composition [9, 10]. An overview of calculated and experimentally obtained values regarding the structural development with increasing AlN content is provided in Fig. 1.5.

Binary CrN appears in a face-centred cubic (fcc) structure. With increasing AlN concentration the Al atoms can substitute the Cr atoms while the crystal still retains its cubic structure. However, at AlN contents of 70.0-77.2 mol% a phase transformation to the hexagonal close packed (hcp) structure of AlN occurs.

The best mechanical and tribological behaviour as well as the highest resistance to oxidation is found for coatings with the maximum AlN concentration while still retaining an fcc structure. While binary CrN and binary AlN have a hardness of ~ 23 GPa [9] and ~ 15 GPa [11], respectively, literature gives hardness values of 27.7-40.8 GPa [9, 12–14] for $\text{Al}_x\text{Cr}_{1-x}\text{N}$ coatings with AlN contents near the transition range. The increase in hardness occurs because of solid solution hardening, with the dissolved Al atoms restraining dislocation movement in the CrN lattice. Only a few publications are available reporting values for the corresponding elastic modulus that are in the region of ~ 350 GPa [13].

Reiter et al. [9] found that the oxidation onset of $\text{Al}_x\text{Cr}_{1-x}\text{N}$ coatings is shifted from 800 to 900-950 °C with increasing AlN content as long as the fcc structure is retained. While CrN is completely oxidised at 1100 °C, only 5% of the $\text{Al}_{0.71}\text{Cr}_{0.29}\text{N}$ film was oxidised at the same temperature [9]. The key processes determining oxidation are the outward diffusion of Cr, Al, and N and the inward diffusion of O. Since Cr diffusion is favoured compared to Al diffusion, the top layer in the oxidised film is mainly composed of Cr_2O_3 [15].

Likewise, coatings with AlN concentrations near 70 mol% reveal the highest resistance against wear. This behaviour was observed for both room temperature and high tem-

perature (500 and 700 °C) testing conditions with alumina balls as counterparts. Wear coefficients of $\text{Al}_{0.62}\text{Cr}_{0.38}\text{N}$ coatings are reported as 10^{-14} and $7 \times 10^{-15} \text{ m}^3\text{N}^{-1}\text{m}^{-1}$ for 700 and 500 °C, respectively, and $10^{-16} \text{ m}^3\text{N}^{-1}\text{m}^{-1}$ for room temperature [16]. The steady-state coefficient of friction (COF) at room temperature is rising with increasing AlN content from 0.4 for binary CrN coatings to 0.7 near the transition range. At testing temperatures of 500 and 700 °C higher values are reported, with an increase in the COF from 0.5 for binary CrN to 1.1 for the $\text{Al}_{0.62}\text{Cr}_{0.38}\text{N}$ coating [16].

1.3.2 The Influence of Alloying Elements

Endrino and Derflinger [17] investigated the influence of transition metals alloyed to AlCr targets on the phase stability and mechanical properties of AlCrN films. The coatings were prepared via cathodic arc evaporation and the targets contained 70 at.% of Al, 25 at.% of Cr and 5 at.% of Ti, V, Y, Nb, Mo, and W, respectively.

All films except the one containing Y presented the cubic structure of CrN and formed equiaxial large grains. The presence of Y hinders the solution of Al into Cr and thus prevents the formation of metastable phases which leads to an amorphous film structure. In the case of the samples alloyed with Mo and W a maximum hardness of 35 GPa was measured. This is due to the strengthening of metastable phases by larger soluble atoms. On the other hand, the coatings containing V and Y only yielded hardness values of 26 GPa. AlCrTiN and AlCrWN exhibited the best performance in oxidation tests. They also showed a high content of Al in the oxidised layer. This suggests the possible formation of Al_xO_y type oxides, which would enhance high temperature material behaviour [17].

Similar research on the influence of Si on the AlCrN system has been performed by Soldán et al. [18]. Different coatings were arc-evaporated from $\text{Al}_{70}\text{Cr}_{30-x}\text{Si}_x$ -targets with $x = 0, 1, 2, 5$ at.%. It was found that for Si contents under 2 at.% in the target the cubic AlCrN phase is stable. At higher Si contents, the fcc phase can only be stabilised utilising high bias voltages during deposition. Beneficial effects of Si on the hardness due to grain refinement are generally restricted to the presence of the cubic AlCrN phase [18, 19].

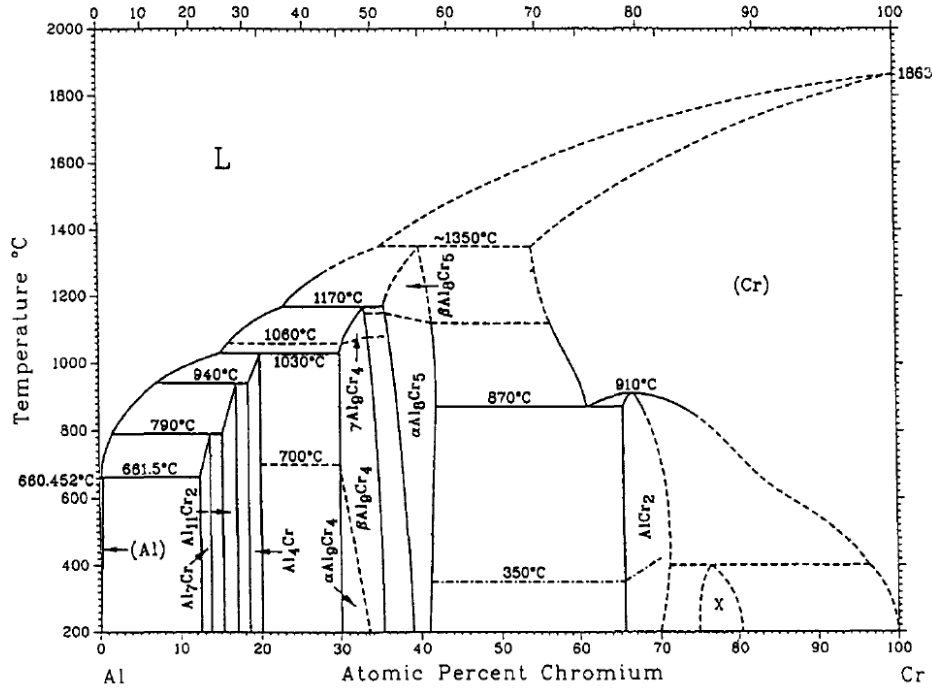


Fig. 1.6: The Al-Cr phase diagram [21].

1.4 Target Fabrication

In general, targets are fabricated either via conventional casting processes or by powder-metallurgical techniques [20]. The alloy system Al-Cr will be used to exemplify both manufacturing routes, since AlCr targets were utilised within the present work.

Casting of metallic alloy-targets is only possible for certain compositions, which are determined by intermetallic phases in the corresponding phase diagram. The casting process is especially complex if a low-melting component such as Al is present. For example, in the case of a target consisting of 30 at.% of Cr and 70 at.% of Al, heating above 1200°C is necessary to achieve the required Cr content, as can be seen in the binary phase diagram in Fig. 1.6. If there is a considerable difference in the melting temperatures and, hence, the vapour pressures of the components, high cooling rates are essential to avoid decomposition during the casting process [20].

On the other hand, powder-metallurgical target production is more flexible and economic. Basically every desired target composition can be achieved by mixing elemental powders (in the present case Al and Cr), which are then compressed into compact moulds. The subsequent heat treatment is called *sintering* and takes place below the melting temperatures of all involved powders. The interaction of surface energy and

Tab. 1.1: Grain size distribution of the elemental powders used for the powder-metallurgical production of the targets utilised within this work.

Material	<32 μm	32-45 μm	45-63 μm	63-80 μm	80-100 μm
	[%]	[%]	[%]	[%]	[%]
Al	75.9	14.6	7.6	1.8	0.1
Cr	2.8	10.9	39.4	46.9	0.0
Fe	99.1	0.8	0.1	0.0	0.0

diffusion at elevated temperatures allows for the development of a solid body with a density of nearly 100% [20, 22]. Alternatively, the densification of the powders can also be achieved by the sole application of pressure, disregarding the sintering step. This process is known as *cold forging* and represents the state of the art in industry for manufacturing AlCr targets.

The targets used for the depositions performed within this work were powder-metalurgically manufactured by Plansee Composite Materials GmbH, Lechbruck, GER. Fe impurities were introduced by adding elemental Fe powder to the Al and Cr powders. As can be seen in the grain size distribution of the powders given in Table 1.1, the majority of the Fe grains is smaller than 32 μm . Microsections of targets with increasing Fe content are shown in Fig. 1.7, where the Cr and Fe grains are visible in the Al matrix. The number of Fe grains is rising with increasing Fe content.

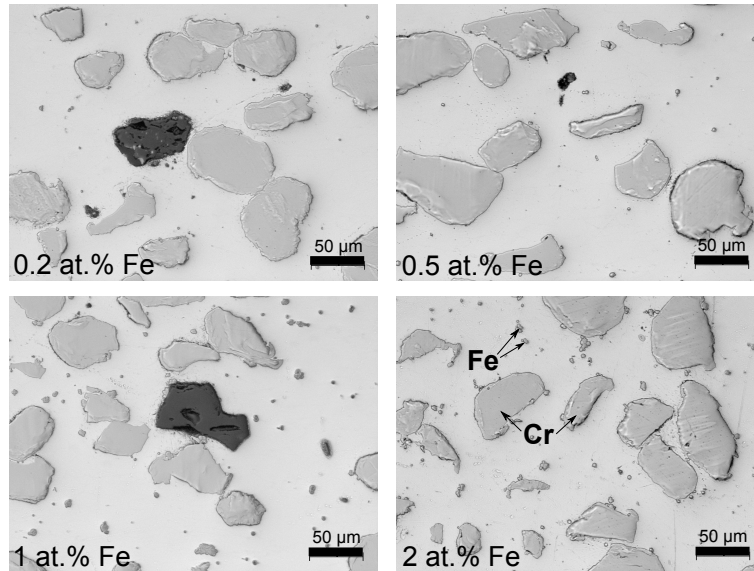


Fig. 1.7: Microsections of AlCr(Fe) targets with increasing Fe content as used within this work.

Bibliography

- [1] A. Anders. *Cathodic Arcs: From Fractal Spots to Energetic Condensation*. Springer Science + Business Media, New York, 2008.
- [2] U. Helmersson, M. Lattemann, J. Bohlmark, A.P. Ehasarian, and J.T. Gudmundsson. Ionized physical vapor deposition (IPVD): A review of technology and applications. *Thin Solid Films*, 513(1-2):1 – 24, 2006.
- [3] D.M. Sanders and A. Anders. Review of cathodic arc deposition technology at the start of the new millennium. *Surface and Coatings Technology*, 133-134:78 – 90, 2000.
- [4] H. Willmann. *Al-Cr-N film design for high temperature applications*. PhD thesis, Montanuniversität Leoben, 2007.
- [5] P.A. Lindfors, W.M. Mularie, and G.K. Wehner. Cathodic arc deposition technology. *Surface and Coatings Technology*, 29(4):275 – 290, 1986.
- [6] M. Ohring. *Materials Science of Thin Films: Deposition and Structure*. Academic Press, San Diego, second edition, 2002.
- [7] J.E. Greene. Thin film nucleation, growth, and microstructural evolution: An atomic scale view. In P.M. Martin, editor, *Handbook of Deposition Technologies for Films and Coatings*, pages 554 – 620. William Andrew Publishing, Boston, third edition, 2010.
- [8] P.B. Barna and M. Adamik. Fundamental structure forming phenomena of polycrystalline films and the structure zone models. *Thin Solid Films*, 317(1-2):27 – 33, 1998.
- [9] A.E. Reiter, V.H. Derflinger, B. Hanselmann, T. Bachmann, and B. Sartory. Investigation of the properties of $Al_{1-x}Cr_xN$ coatings prepared by cathodic arc evaporation. *Surface and Coatings Technology*, 200(7):2114 – 2122, 2005.
- [10] Y. Makino. Prediction of phase change in pseudobinary transition metal aluminum nitrides by band parameters method. *Surface and Coatings Technology*, 193(1-3):185 – 191, 2005.
- [11] Y.A. Ide, T.B. Nakamura, and K.C. Kishitake. Formation of Al-Cr-N films by a DC reactive sputtering method and evaluation of their properties. In B. Mishra, editor, *Proceedings of the Second International Conference on Processing Materials for Properties*, pages 291–296, San Francisco, CA, 2000.
- [12] J.L. Endrino, G.S. Fox-Rabinovich, and C. Gey. Hard AlTiN, AlCrN PVD coatings for machining of austenitic stainless steel. *Surface and Coatings Technology*, 200(24):6840 – 6845, 2006.

- [13] R. Franz, J. Neidhardt, B. Sartory, R. Kaindl, R. Tessadri, P. Polcik, V.H. Derflinger, and C. Mitterer. High-temperature low-friction properties of vanadium-alloyed AlCrN coatings. *Tribology Letters*, 23(2):101–107, 2006.
- [14] G.S. Kim and S.Y. Lee. Microstructure and mechanical properties of AlCrN films deposited by CFUBMS. *Surface and Coatings Technology*, 201(7):4361 – 4366, 2006.
- [15] A.E. Reiter, C. Mitterer, M. Ante, and B. Sartory. Oxidation of arc-evaporated $\text{Al}_x\text{Cr}_{1-x}\text{N}$ coatings. *Journal of Vacuum Science and Technology A*, 25(4):711–720, 2007.
- [16] R. Franz, B. Sartory, R. Kaindl, R. Tessadri, A. Reiter, V.H. Derflinger, P. Polcik, and C. Mitterer. High-temperature tribological studies of arc-evaporated $\text{Al}_x\text{Cr}_{1-x}\text{N}$ coatings. In G. Kneringer, P. Rödhammer, and H. Wildner, editors, *16th Int. Plansee Seminar*, volume 2, pages 932–945, Reutte (A), 2005.
- [17] J.L. Endrino and V. Derflinger. The influence of alloying elements on the phase stability and mechanical properties of AlCrN coatings. *Surface and Coatings Technology*, 200(1-4):988 – 992, 2005.
- [18] J. Soldán, J. Neidhardt, B. Sartory, R. Kaindl, R. Cerstvý, P.H. Mayrhofer, R. Tessadri, P. Polcik, M. Lechthaler, and C. Mitterer. Structure-property relations of arc-evaporated Al-Cr-Si-N coatings. *Surface and Coatings Technology*, 202(15):3555 – 3562, 2008.
- [19] J.L. Endrino, S. Palacín, M.H. Aguirre, A. Gutiérrez, and F. Schäfers. Determination of the local environment of silicon and the microstructure of quaternary CrAl(Si)N films. *Acta Materialia*, 55(6):2129 – 2135, 2007.
- [20] Oerlikon Trading AG. Verfahren zum Herstellen von Metalloxidschichten durch Funkenverdampfung. European Patent Office EP 2 166 128 A1, 2010.
- [21] M. Audier, M. Durand-Charre, E. Laclau, and H. Klein. Phase equilibria in the Al-Cr system. *Journal of Alloys and Compounds*, 220(1-2):225 – 230, 1995.
- [22] Plansee SE. <http://www.plansee.at/pulvermetallurgie.htm>, August 2011.

2 Manuscript

Influence of Fe impurities on structure and properties of AlCrN films grown by cathodic arc evaporation

M. Mühlbacher^{1,2}, R. Franz², M. Lechthaler³, P. Polcik⁴, C. Mitterer^{1,2}

1 Christian Doppler Laboratory for Advanced Hard Coatings at the Department of Physical Metallurgy and Materials Testing, Montanuniversität Leoben, Franz-Josef-Strasse 18, 8700 Leoben, Austria

2 Chair of Functional Materials and Materials Systems, Department of Physical Metallurgy and Materials Testing, Montanuniversität Leoben, Franz-Josef-Strasse 18, 8700 Leoben, Austria

3 OC Oerlikon Balzers AG, Iramali 18, 9496 Balzers, Principality of Liechtenstein

4 PLANSEE Composite Materials GmbH, Siebenbürgerstrasse 23, 86983 Lechbruck am See, Germany

Abstract

The influence of Fe impurities with contents of up to 2 at.% in AlCr targets on the properties of arc-evaporated AlCr(Fe)N coatings was investigated. Analyses of the synthesised coatings by electron microscopy and X-ray diffraction reveal no significant changes in the microstructure. The incorporated Fe atoms are homogeneously distributed and substitute Cr and Al atoms in the crystal lattice as suggested by elemental mappings and X-ray photoelectron spectroscopy. No pronounced modification of the mechanical properties is evident. However, thermogravimetric analysis in oxygen containing atmosphere reveals a lower oxidation onset temperature for the coatings with incorporated Fe. A chemical analysis of oxidised coatings by Raman spectroscopy discloses the formation of Cr₂O₃ at 800 to 900 °C if Fe is present in the coating. This lower oxidation onset results in a slightly reduced wear resistance at temperatures up to 700 °C. In contrast, the presence of Fe delays the oxidation reaction at temperatures exceeding 1000 °C, presumably due to the formation of a dense oxide scale protecting the coating from further oxidation.

KEY WORDS: AlCrN, CrAlN, Fe impurities, cathodic arc evaporation, hard coatings, physical vapour deposition

1 Introduction

AlCrN has been established as a protective hard coating due to its superior mechanical and tribological properties compared to binary nitride coatings. These properties are closely connected to the chemical composition and resulting structure of the coating [1]. The solubility limit of AlN in the face-centred cubic (fcc) CrN phase is reported to be 70-77 mol% [1-3], while at higher AlN contents a transformation to the hexagonal wurtzite type structure of AlN occurs, generally resulting in a degradation of the coating's performance [1]. The best mechanical and tribological behaviour as well as the highest resistance to oxidation is found for coatings with the maximum AlN concentration while still retaining the fcc structure [1, 4, 5]. Hardness values reported in literature for Al_{0.71}Cr_{0.29}N coatings are in the range of 27.7-40.8 GPa [1, 6, 7], with

the dissolved Al atoms restraining dislocation movement in the CrN lattice. Moreover, the oxidation onset of fcc- $\text{Al}_x\text{Cr}_{1-x}\text{N}$ coatings is shifted from 800 °C to 900-950 °C with increasing AlN content [4]. In combination with its high thermal stability, these facts account for the excellent wear resistance of AlCrN even at elevated temperatures [5].

Basically, there are two approaches of synthesising AlCrN films by means of physical vapour deposition: The use of pure Al and Cr targets is widely reported in literature [2, 7–10], but deposition from alloyed AlCr targets [1, 11–14] is more common in industrial applications, allowing for the specific tailoring of film composition by adjusting the Al/Cr ratio in the targets. The most economic and flexible way of manufacturing alloyed metallic targets is by means of powder metallurgy, which also represents the state of the art in industry. However, due to the complex and interrelated nature of the metal commodity markets, it is often difficult to ensure a consistent degree of purity of the elemental powders that are the basis of all powder-metallurgically fabricated products. In the present case, especially Fe impurities in the Al and Cr powders pose a challenge to target manufacturers. Although research has been performed on the influence of transition metals (Ti, V, Y, Nb, Mo, W) [14, 15] as well as Si [16, 17] alloyed to AlCr targets on the phase stability and mechanical properties of AlCrN films, there is a lack of literature reporting possible effects of Fe on the deposition process or film properties.

Therefore, the aim of the present work is to study the microstructural development, the mechanical and tribological properties as well as the oxidation resistance of AlCr(Fe)N coatings as a function of the Fe content in the targets. In addition, special emphasis is placed on the analysis of the oxidation behaviour.

2 Experimental Details

AlCr(Fe)N coatings were synthesised in an Oerlikon Balzers INNOVA industrial-scale cathodic arc evaporation device with a base pressure in the lower range of 10^{-3} Pa. The substrates, including high speed steel (DIN 1.3343, AISI M2) coupons (\varnothing 30 mm \times 10 mm), a low-alloyed steel (DIN 1.0330, AISI 1008), Si(100), and Fe foil, were mounted on a two-fold planetary rotating carousel. Prior to deposition the substrates were plasma heated to 500 °C and etched in a pure Ar plasma. During deposition the substrate bias voltage was kept constant at -40 V and the nitrogen gas pressure was set to 3.5 Pa. Four arc sources were equipped with powder-metallurgically manufactured AlCrFe targets with Fe contents of 0, 0.2, 0.5, 1, and 2 at.%, respectively (see Table 1) and operated with 150 A each. It has to be noted at this point that naturally even the binary AlCr targets contained a certain degree of Fe impurities (<0.04 at.%). Two deposition series with deposition times of 60 min and 30 min were performed, resulting in a film thickness of ~ 3.2 μm and ~ 1.3 μm , respectively.

The morphology of the resulting coatings was studied by energy-filtered transmission electron microscopy (TEM) using a FEI Tecnai TF20 TEM. Elemental maps of Al, Cr, Fe and N were recorded employing the jump-ratio technique according to Ref. [18]. Images of the film surfaces were taken with a Zeiss EVO 50 scanning electron microscope (SEM) with an acceleration voltage of 20 kV. The chemical composition of the coatings was analysed by energy dispersive X-ray spectroscopy (EDX) with an Oxford Instruments INCA EDX detector connected to the SEM. Insights into the chemical bonding structure were provided by X-ray photoelectron spectroscopy (XPS) using an Omicron Multiprobe system with a monochromised Al K_{α} beam (1486.6 eV) with a resolution <0.5 eV. Prior to the measurements the samples were heated to 350 °C to remove volatile surface contaminants while retaining the initial surface bonding structure. The characterisation of the crystal structure was performed by X-ray diffraction (XRD) with a Bruker-AXS D8 Advance diffractometer with parallel beam geometry using Cu K_{α} radiation and an energy-dispersive SolX detector from Bruker-AXS via scans in Bragg-Brentano and grazing incidence (2°) mode.

Hardness and Young's modulus were calculated according to Oliver and Pharr [19] from load-displacement curves measured in a UMIS nanoindenter equipped with a Berkovich tip at maximum loads ranging from 5 to 20 mN. The biaxial stress state of the coatings was determined by means of the cantilever beam bending technique of Si stripes (20 mm \times 7 mm \times 0.525 mm) as described in Ref. [20].

The oxidation behaviour of the AlCr(Fe)N coatings was investigated by thermogravimetric analysis (TGA). The coatings were chemically removed from the Fe foil using diluted nitric acid. Subsequently, the material was mechanically ground to a fine powder whereof 25-50 mg were analysed in a Setsys EVO 2400 device. Dynamical heating with a heating rate of 10 K/min to a maximum temperature of 1500 °C was performed in an atmosphere of synthetic air (50 ml/min). A rerun of the measurements with the same parameters was conducted to check if the samples were fully oxidised. For further investigations samples were annealed in ambient atmosphere for 1 hour at temperatures of 800, 900 and 1000 °C. Subsequently, the oxidised coatings were analysed by Raman spectroscopy at 3 spots evenly distributed on the sample surface with a HORIBA Jobin Yvon LabRam-HR800 confocal spectrometer, employing a Nd:YAG laser (wavelength 532 nm) for excitation. The Raman signal was detected with a CCD-camera using a 100 \times objective.

Tribological tests were performed at room temperature (RT), 500, and 700 °C with a ball-on-disc tribometer from CSM Instruments using alumina balls (\varnothing 6 mm) as counterparts. The normal load was kept constant at 5 N and the sliding speed was set to 10 cm/s. The sliding distance was 300 m and the radius of the wear track 7 mm for all tests. No lubricant was applied. The wear tracks were subsequently investigated with a Wyko NT 1000 optical 3D white light profiling system.

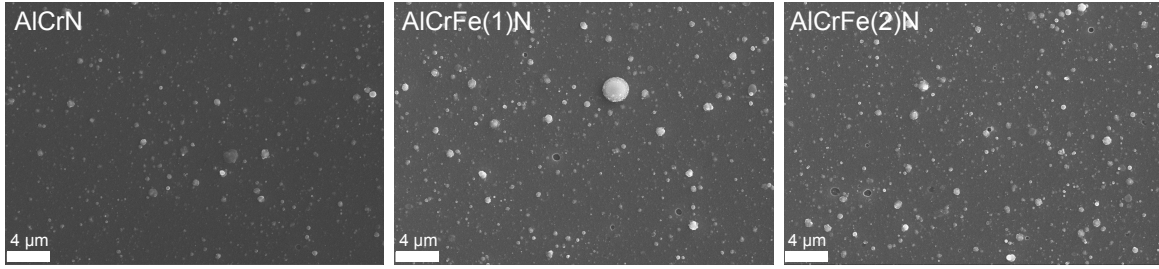


Fig. 1: SEM micrographs of the film surfaces of the standard AlCrN coating and the coatings deposited from targets containing 1 and 2 at.% of Fe (AlCrFe(1)N and AlCrFe(2)N, respectively).

3 Results

3.1 Morphology, chemical composition and structure

All coatings exhibit a greyish colour and are well adherent on metal substrates. The arithmetic surface roughness R_a is in the range of 10-20 nm and can be related to droplet and macroparticle formation as a typical feature of the arc evaporation process. No apparent change in droplet density or size can be observed for coatings with Fe contaminations compared to the standard AlCrN coating as displayed in Fig. 1.

A detailed analysis of the morphology of the coating with the highest Fe content is provided by TEM. Fig. 2(a) shows a bright-field image of the cross-section revealing a dense, nanocolumnar microstructure. An increase in grain size with increasing distance to the substrate can be noticed which is due to the transition from the nucleation phase to steady-state growth. The morphology is comparable to a Fe-free $\text{Al}_{0.71}\text{Cr}_{0.29}\text{N}$ film shown in [1]. Elemental mappings of Al, Cr, Fe, and N as displayed in Fig. 2(b-f) exhibit a homogeneous distribution of all elements throughout the coating. No preferential Fe enrichment along grain boundaries is observable within the resolution limits. This indicates that Fe atoms are substitutionally incorporated

Tab. 1: Chemical composition of the AlCr(Fe)N coatings as analysed by EDX. The notations of the individual films will be used throughout the paper.

Target Al/Cr/Fe [at.%]	Coating				Notation of films
	Al [at.%]	Cr [at.%]	Fe [at.%]	N [at.%]	
70/30/0	34.0	15.6	-	50.4	AlCrN
69.9/29.9/0.2	33.7	16.9	-	49.4	AlCrFe(0.2)N
69.75/29.75/0.5	34.2	16.3	-	49.5	AlCrFe(0.5)N
69.5/29.5/1	32.7	15.3	0.5	51.5	AlCrFe(1)N
69/29/2	31.9	15.5	1.3	51.3	AlCrFe(2)N

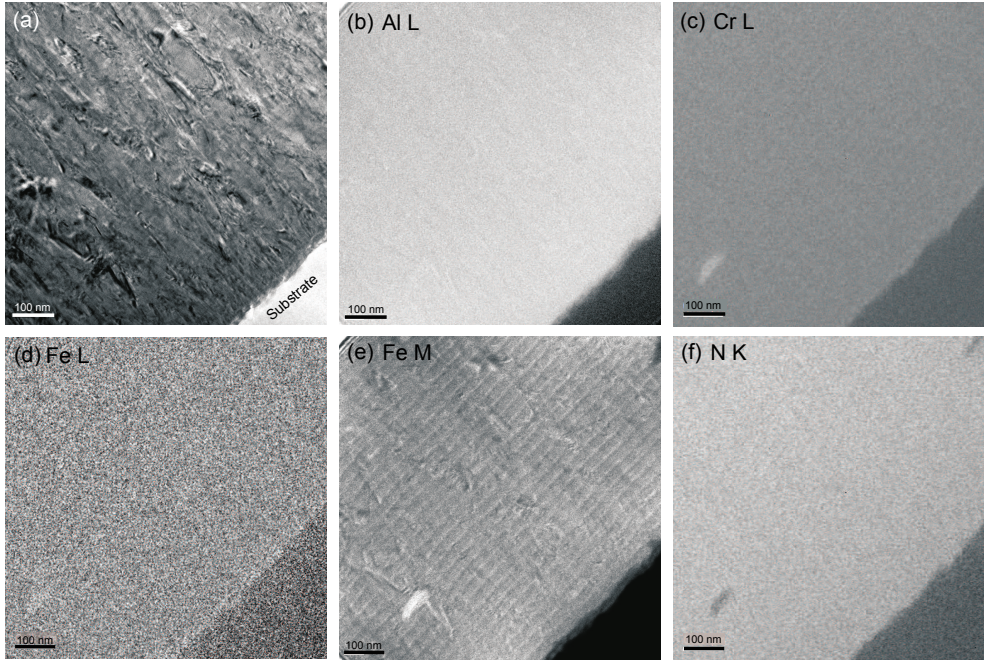


Fig. 2: (a) Bright-field cross-sectional TEM image of the coating deposited from $\text{Al}_{0.69}\text{Cr}_{0.29}\text{Fe}_{0.02}$ targets and (b-f) elemental mappings of the same coating acquired by the jump-ratio technique.

into the crystal lattice. The layered structure apparent in the images obtained from the Cr L-edge (Fig. 2c) and Fe M-edge (Fig. 2e) is due to compositional variations because of the substrate rotation during deposition [21].

The chemical composition as measured by EDX is given in Table 1. All coatings can be considered stoichiometric, with an N content of ~ 50 at.% suggesting the absence of intermetallic phases. Fe contents in the coatings are within the EDX detection range only for the two target systems with the highest level of Fe impurities. In these cases, the Fe content in the films corresponds well to the target composition. However, the $\text{Al}/(\text{Cr}+\text{Fe})$ ratio in the films is considerably lower than in the targets. This fact was previously reported [16, 22] and is presumably due to gas scattering during the deposition process.

The bonding structure of $\text{AlCr}(\text{Fe})\text{N}$ was investigated by XPS, which primarily addresses the nearest neighbour configuration. All relevant core level spectra of the reference AlCrN coating as well as the $\text{AlCrFe}(1;2)\text{N}$ films have been analysed, but the main focus is placed on the bonding state of Fe. A separation in energy between the $2p_{1/2}$ and $2p_{3/2}$ core level spectra of Fe2p can be observed in Fig. 3, which is a result of spin-orbit coupling. In case of Fe-N only a few references could be found in literature reporting binding energies in the range of 707.1-710.7 eV [23-25]. In the present study the main contribution to the Fe2p $_{3/2}$ spectra of the Fe containing coatings (Fig. 3) is detected at 709.5 eV, and can therefore be assigned to Fe-N bonds. At higher binding energies Fe-O bonds may contribute to the spectra, indicating

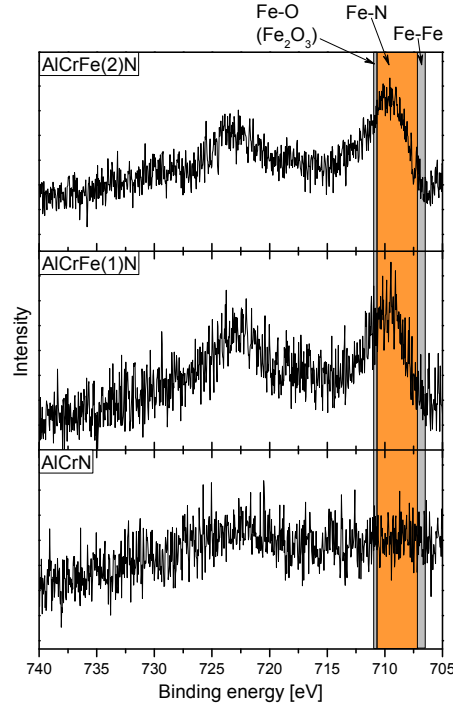


Fig. 3: Fe_{2p} XPS core level spectra of AlCr(Fe)N coatings. Relevant binding energy ranges are given according to Refs. [23–30].

that Fe on the surface is oxidised. Relevant published binding energies are in the range of 710.5–711.0 eV [26–28] in case of Fe₂O₃. No contributions of Fe-Fe bonds with a binding energy of 706.5–707.2 eV [27, 29, 30] can be observed in Fig. 3 and an examination of the Al_{2s} and Cr_{2p} spectra also reveals the absence of Al-Al and Cr-Cr bonds, respectively. The N_{1s} core level spectra (not shown) complement these findings. They exhibit only one contribution at 396.5 eV attributed to N-(Al,Cr,Fe) bonds, which show an indistinguishable overlap in the binding energies as reported in [22, 23]. Therefore, no difference between the standard AlCrN coating and the Fe containing films can be noticed in the N_{1s} spectra.

The XRD patterns displayed in Fig. 4 show that all coatings exclusively exhibit reflections attributed to the fcc-AlCrN structure regardless of the Fe content. According to the rule of mixture, the diffraction peaks are located between the reflections of fcc-CrN [31] and fcc-AlN [32]. Since the Al concentration in the coatings is roughly twice the Cr concentration, it is expected that the diffraction peaks appear closer to the AlN reflections than to the corresponding CrN reflections. The slight deviation to smaller diffraction angles apparent in Fig. 4 can presumably be related to residual stresses in the coatings. Crystallite sizes have been calculated by analysing the (200) reflections applying a Pseudo-Voigt function as described in Ref. [33]. The obtained results range from 20 to 30 nm without a correlation with the Fe concentration in the coatings.

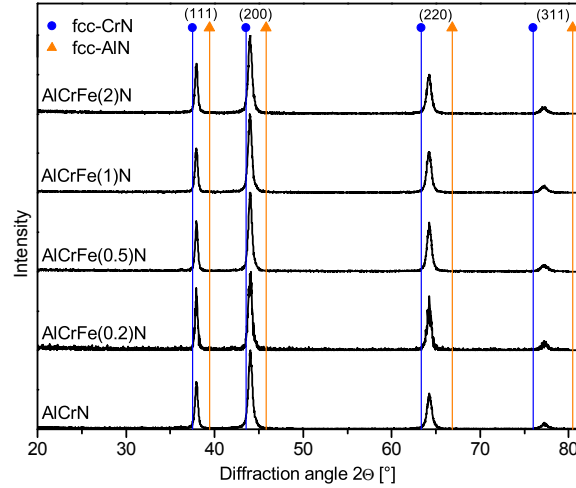


Fig. 4: XRD patterns of AlCr(Fe)N coatings with increasing Fe concentration. Reference peak positions for fcc-CrN [31] and fcc-AlN [32] are included.

3.2 Mechanical properties

Fe concentrations of up to 2% in the targets seem to have no pronounced influence on the hardness of the coatings, which is ranging from 31 to 33 GPa. These results are in the lower range of hardness values reported in literature [1, 6, 7, 34] for comparable Fe-free AlCrN coatings. The corresponding Young's modulus ranges from 320 to 360 GPa. Only the AlCrFe(0.5)N coating shows an increased elastic modulus of ~ 380 GPa.

Biaxial stress temperature measurements were performed to investigate the stress state of the synthesised coatings. Residual stresses in the coatings are generally compressive. In the as-deposited state values of -2.1 GPa for coatings with low contents of Fe are obtained. A decrease to values of approximately -1.9 GPa and -1.8 GPa is observed for the AlCrFe(1)N and AlCrFe(2)N coating, respectively. At deposition temperature (500 °C) the coatings show a similar behaviour, with residual stresses of -3.9 GPa for coatings with low Fe contents and a reduction to -3.7 GPa and -3.2 GPa for the AlCrFe(1)N and AlCrFe(2)N coating, respectively. These values mainly represent the intrinsic stresses, as the contribution of thermal stresses vanishes at deposition temperature.

3.3 Oxidation behaviour

TGA measurements in synthetic air were conducted to investigate the influence of Fe impurities on film oxidation. Samples were prepared as fine powders to obtain a high specific surface, promoting the oxidation reaction. EDX measurements revealed that the Fe content in the powders is in accordance with Fe concentrations in the coatings (Table 1). All samples show a pronounced mass increase with rising temperature as displayed in Fig. 5(a), which can be

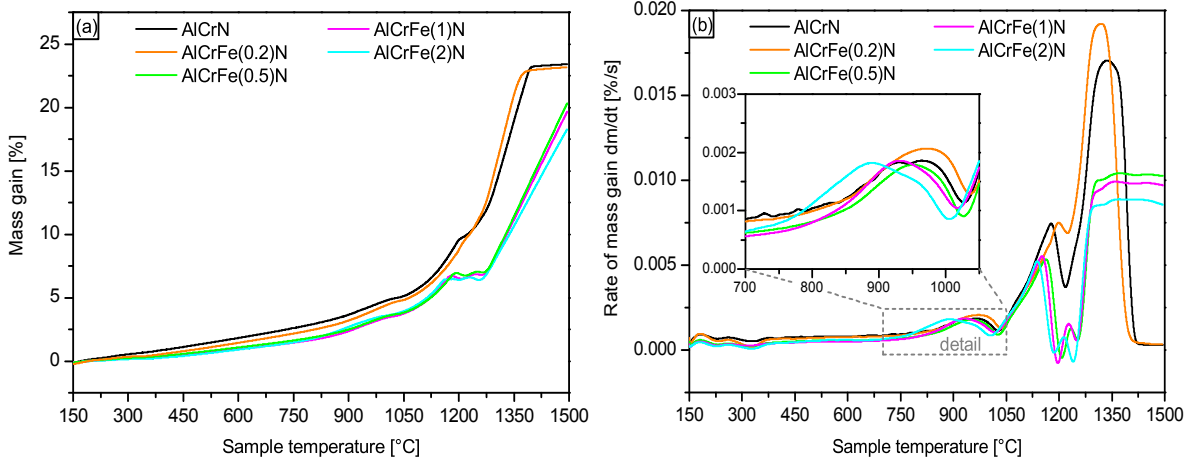


Fig. 5: (a) TGA measurements of powdered AlCr(Fe)N films in synthetic air at a heating rate of 10 K/min and (b) the first derivative of the TGA signal representing the rate of mass gain.

related to the formation of oxides. However, while curves representing the standard AlCrN as well as the AlCrFe(0.2)N specimen level off at a temperature of ~ 1350 °C with a total mass gain of $\sim 23\%$, the reaction seems to be delayed in case of the coatings with higher Fe contents. This difference is due to the appearance of a plateau in the corresponding curves between temperatures of 1200 and 1300 °C, resulting in an overall lower mass increase up to the maximum annealing temperature. More insights are provided by the first derivative of the TGA signal shown in Fig. 5(b), with the areas under the curves representing the reaction specific mass gain. In case of the AlCrFe(2)N specimen a first significant mass gain occurs at a temperature of 800-900 °C while for the other samples it is shifted to higher temperatures of 900-1000 °C (see the detail in Fig. 5b). A more pronounced increase in the rate of mass gain arises slightly below 1050 °C for all samples. In case of the AlCrFe(0.5;1;2)N specimens the mass gain subsequently comes to a standstill relating to the plateau observable in Fig. 5(a). A similar behaviour, though less distinctive, can be noticed in Fig. 5(b) for the reference AlCrN sample, while in case of the AlCrFe(0.2)N powder it is almost completely suppressed. With a further increase in temperature again a strong rise in the rate of mass gain occurs, which starts at ~ 1200 °C for the AlCrN sample but is shifted to higher temperatures with increasing Fe content in the powders. While the AlCrN as well as the AlCrFe(0.2)N specimen seem to be completely oxidised at ~ 1350 °C, the rate of mass gain is still almost constant at ~ 0.01 %/s in case of the AlCrFe(0.5)N sample and decreases with rising Fe concentration in the powders.

XRD measurements performed on the powders after TGA reveal the formation of (Al,Cr) $_2$ O $_3$ -type oxides regardless of the Fe content. However, to investigate the shift of oxidation onset to lower temperatures with increasing Fe content as suggested in Fig. 5(b) in more detail, all

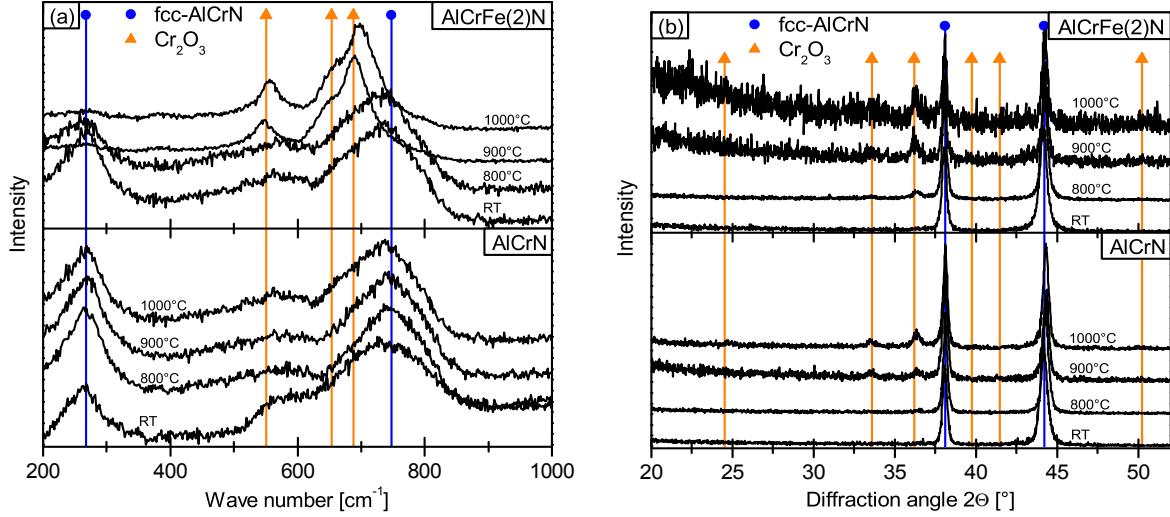


Fig. 6: (a) Raman spectra and (b) XRD patterns obtained after annealing of AlCr(Fe)N in ambient air. Reference XRD peak positions for Cr₂O₃ [35] are included as well as Raman peak positions from Ref. [16] for fcc-AlCrN and Ref. [36] for Cr₂O₃.

coatings were annealed in ambient atmosphere for 1 hour at temperatures of 800, 900 and 1000 °C. Fig. 6(a) shows a comparison of Raman spectra obtained from the reference AlCrN and the AlCrFe(2)N coating. Up to 1000 °C no oxidation of the AlCrN coating can be detected, while the AlCrFe(2)N coating already seems to be completely covered by a Cr₂O₃ surface layer at 900 °C. The effect of Fe on the oxidation onset is observable by Raman spectroscopy even for very low Fe concentrations and can already be noticed in case of the AlCrFe(0.2)N coating (spectrum not shown) with the formation of Cr₂O₃ between 900 and 1000 °C.

Since Raman spectroscopy provides only localised information, additional measurements have been performed by XRD, where a larger sample volume is investigated. First indications of the development of oxides are found at a temperature of 800 and 900 °C for the standard and the AlCrFe(2)N film, respectively, as displayed in Fig. 6(b). The low-intensity and broad peaks between 30° and 40° in the XRD patterns suggest the formation of a Cr₂O₃ phase with low crystallinity. Up to 1000 °C no Al₂O₃ phase could be detected on either sample. Despite the partial delamination of AlCrFe(2)N films at higher annealing temperatures and the somewhat noisy XRD signal, it is obvious that the intensity of the peaks related to Cr₂O₃ increases with increasing Fe concentration. Still, in all cases the overall fraction of the Cr₂O₃ phase is small compared to the AlCr(Fe)N phase. These findings correlate well with the results obtained by TGA regarding the oxidation onset temperature.

3.4 Tribological properties

In tribological experiments the evolution of the coefficient of friction (COF) with the sliding distance is recorded. Since the COF can strongly depend on temperature, tests were performed at RT, 500 and 700 °C. Values for the steady state COF at RT are found to be 0.5-0.6 independent of the Fe content in the coating. They are slightly lower than values reported in literature [11] for comparable films. At elevated temperatures the COF of the reference AlCrN coating rises to ~ 0.7 . In case of the AlCrFe(0.2)N coating the increase to values of 0.9-1.0 is more pronounced but no further increase can be observed for the coatings with higher Fe concentrations.

3D profiles of the wear tracks after testing are shown in Fig. 7, with the AlCrFe(1)N film exemplifying the Fe containing coatings. At RT all coatings show almost no visible wear track after a sliding distance of 300 m. At 500 °C the abrasion is most pronounced in the centre of the wear tracks, where a narrow, deep depression is formed, while at 700 °C abrasion is more uniform. At both temperatures an increasing wear depth is observable even for the film with the lowest Fe content compared to the reference coating, but no further increase can be noticed with rising Fe concentrations in the coatings within the studied range.

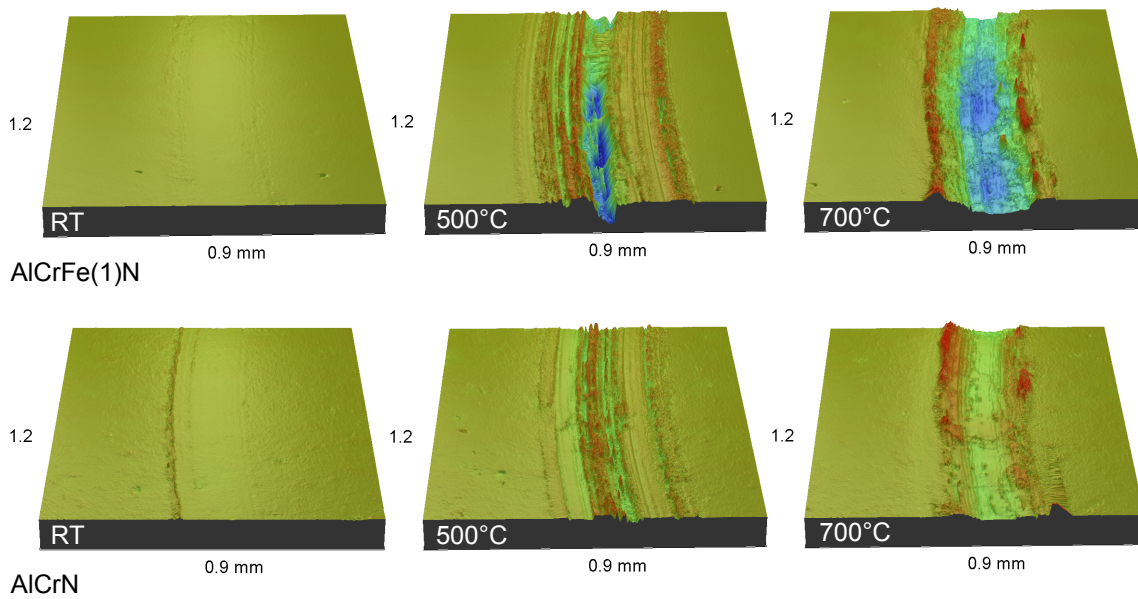


Fig. 7: 3D images obtained by optical profilometry of wear tracks on the standard AlCrN coating (below) and the AlCrFe(1)N coating (above) after ball-on-disc tests against Al_2O_3 at different temperatures.

4 Discussion

Fe impurities of up to 2 at.% in the AlCr targets seem to have no effect on the morphology or microstructure of the deposited AlCr(Fe)N coatings. An fcc structure is retained for all investigated coatings, which is in good agreement with the maximum solubility of AlN in fcc-CrN as reported in [1–3]. XPS measurements reveal no contributions of Me-Me bonds (Me = Al,Cr,Fe), which suggests the absence of intermetallic compounds. Therefore, the coatings have to be seen as a solid solution of (Al,Cr,Fe)N, as complemented by the stoichiometry obtained by EDX. Presumably, Fe atoms are substitutionally incorporated into the crystal on Cr or Al lattice sites. Since the atomic radii of Fe and Cr are nearly identical [37], the dissolution of Fe induces almost no additional strain which would hinder dislocation movement in the film. Therefore, no pronounced influence of the studied small Fe contents on the hardness of the coatings can be detected.

On the other hand, the effect of Fe incorporation on the oxidation behaviour of the coatings is noticeable. Standard AlCrN coatings form a dense Cr₂O₃-rich oxide surface layer above 900 °C in ambient atmosphere. This prevents further diffusion of oxygen into the bulk film, thereby enhancing oxidation resistance [4]. Lin et al. [10] investigated the underlying decomposition and oxidation reactions in case of an Al_{0.60}Cr_{0.40}N film. It was found that at temperatures between 800 and 900 °C decomposition of the fcc-AlCrN phase accompanied by the formation of a Cr₂O₃ layer commences, which can be qualitatively expressed as:



The reference AlCrN film examined in the present study shows the oxidation onset at higher temperatures, which can be explained by the increased Al content. While the bonding characteristics in fcc-AlN are mainly covalent, the fcc-CrN bonding is basically metallic, resulting in a weaker bond [10, 12]. Therefore, a higher amount of Al atoms will increase the thermal stability of the coating.

This initial oxidation stage can be related to the beginning mass gain at ~900 °C observable in Fig. 5(a). The low rate of mass gain (Fig. 5b) indicates that the oxidation reaction is still mainly controlled by the slow outward diffusion of metallic ions. The formation of a Cr₂O₃ surface layer is confirmed by Raman spectroscopy and XRD in Fig. 6(a,b). With rising temperatures the precipitation of the hexagonal AlN phase occurs as reported in [10], causing a significant decrease in the fraction of fcc-AlN bonds. Subsequently, the formation of a crystalline (Al,Cr)₂O₃ phase [4, 10] results in a rising amount of grain boundary phase as well as the

development of microcracks in the oxidised layer [10]. This enhances the inward diffusion of O, therefore promoting the oxidation reaction as observable in Fig. 5(b) by the rapidly increasing rate of mass gain above ~ 1050 °C.

The influence of Fe impurities on the process first becomes obvious by the shift of the oxidation onset to lower temperatures displayed in Fig. 6. Addition of Fe seems to promote the initial formation of a Cr_2O_3 surface layer. It can be assumed that like Cr and Al, Fe will also form sesquioxides. Fe_2O_3 and Cr_2O_3 show complete miscibility [38], while this is not the case for Fe_2O_3 and Al_2O_3 [39]. Therefore, the addition of Fe leads to a somewhat sooner oxidation onset but might also support the formation of a denser Cr_2O_3 surface layer, which can act as an effective diffusion barrier in later oxidation stages. The effect of Fe on the oxidation resistance of AlCrN coatings could indeed be similar to that of Y [14], which acts as a reactive element, generally triggering the selective oxidation of a component and/or retarding the oxide scale growth. In the present study, this behaviour is most pronounced for the AlCrFe(0.5;1;2)N coatings at temperatures between 1200 °C and 1300 °C, where the mass gain actually comes to a complete standstill (Fig. 5a). This suggests that Fe impurities in the films lead to an enhanced density of the oxidised layer, thereby blocking diffusion paths for the native Al and Cr ions and retarding the overall oxide scale growth. Only when the thermal activation becomes sufficient at ~ 1300 °C the oxidation reaction is resumed. Still, an influence of Fe can be noticed by the decreasing rate of mass gain displayed in Fig. 5(b) for the AlCrFe(2)N sample compared to the AlCrFe(0.5;1)N films. The retarding effect of Fe on the diffusion processes determining the oxidation rate is such that while the reference AlCrN specimen is completely oxidised at ~ 1350 °C, the oxidation reaction is still under way in films with Fe impurities at 1500 °C. However, this behaviour cannot be observed in the case of AlCrFe(0.2)N, where the Fe content in the coating obviously is not sufficient to promote an improved oxide layer density compared to the reference AlCrN film.

The wear behaviour is closely connected to the mechanical properties and the oxidation resistance of the coating depending on the testing temperature. At RT no dependence of the wear depth on the Fe content can be observed, which is in good agreement with the constant hardness values of 31 to 33 GPa obtained for all coatings studied within this work. However, the addition of Fe leads to a lower oxidation onset temperature, which results in more pronounced wear tracks (Fig. 7) for AlCr(Fe)N coatings compared to standard AlCrN films at elevated temperatures.

5 Conclusion

In conclusion it can be stated that Fe contents within the studied range have no pronounced influence on the solubility, morphology and mechanical properties of AlCr(Fe)N coatings. No

preferential enrichment of Fe at grain boundaries can be detected within the TEM resolution limit. Results from EDX and XPS measurements suggest the substitutional incorporation of Fe atoms into the crystal on Al or Cr lattice sites. The influence of Fe on the oxidation behaviour is twofold. Firstly, it leads to a shift of the oxidation onset to 800 °C in case of AlCrFe(2)N as compared to 900-1000 °C for the reference AlCrN coating. This is also related to the tribological properties, where deeper wear tracks are observable at 700 °C if Fe is present in the coating. Secondly, a sufficient amount of Fe seems to promote the formation of a dense Cr₂O₃-rich surface layer, which can act as an effective diffusion barrier. In this case an overall delay of the oxidation reaction occurs at temperatures exceeding 1000 °C.

Acknowledgements

The authors are grateful to Ilse Letofsky-Papst (Austrian Centre for Electron Microscopy and Nanoanalysis, Graz) for TEM investigations and to Alexander Fian (Institute of Nanostructured Materials and Photonics, Weiz, Austria) for XPS measurements. Special thanks go to Paul Mayrhofer for fruitful discussions regarding the TGA measurements. Financial support by the Christian Doppler Research Association is highly acknowledged.

References

- [1] A.E. Reiter, V.H. Derflinger, B. Hanselmann, T. Bachmann, and B. Sartory. Investigation of the properties of $\text{Al}_{1-x}\text{Cr}_x\text{N}$ coatings prepared by cathodic arc evaporation. *Surface and Coatings Technology*, 200(7):2114 – 2122, 2005.
- [2] Y. Makino and K. Nogi. Synthesis of pseudobinary Cr-Al-N films with B1 structure by rf-assisted magnetron sputtering method. *Surface and Coatings Technology*, 98(1-3):1008 – 1012, 1998.
- [3] Y. Makino. Prediction of phase change in pseudobinary transition metal aluminum nitrides by band parameters method. *Surface and Coatings Technology*, 193(1-3):185 – 191, 2005.
- [4] A.E. Reiter, C. Mitterer, M. Ante, and B. Sartory. Oxidation of arc-evaporated $\text{Al}_x\text{Cr}_{1-x}\text{N}$ coatings. *Journal of Vacuum Science and Technology A*, 25(4):711–720, 2007.
- [5] A.E. Reiter, C. Mitterer, M. Rebelo de Figueiredo, and R. Franz. Abrasive and adhesive wear behavior of arc-evaporated hard coatings. *Tribology Letters*, 37:605–611, 2010.
- [6] R. Franz, J. Neidhardt, B. Sartory, R. Kaindl, R. Tessadri, P. Polcik, V.H. Derflinger, and C. Mitterer. High-temperature low-friction properties of vanadium-alloyed AlCrN coatings. *Tribology Letters*, 23(2):101–107, 2006.
- [7] G.S. Kim and S.Y. Lee. Microstructure and mechanical properties of AlCrN films deposited by CFUBMS. *Surface and Coatings Technology*, 201(7):4361 – 4366, 2006.
- [8] O. Knotek, M. Atzor, A. Barimani, and F. Jungblut. Development of low temperature ternary coatings for high wear resistance. *Surface and Coatings Technology*, 42(1):21 – 28, 1990.
- [9] J. Vetter, E. Lugscheider, and S.S. Guerreiro. (Cr:Al)N coatings deposited by the cathodic vacuum arc evaporation. *Surface and Coatings Technology*, 98(1-3):1233 – 1239, 1998.
- [10] J. Lin, B. Mishra, J.J. Moore, and W.D. Sproul. A study of the oxidation behavior of CrN and CrAlN thin films in air using DSC and TGA analyses. *Surface and Coatings Technology*, 202(14):3272 – 3283, 2008.
- [11] R. Franz, B. Sartory, R. Kaindl, R. Tessadri, A. Reiter, V.H. Derflinger, P. Polcik, and C. Mitterer. High-temperature tribological studies of arc-evaporated $\text{Al}_x\text{Cr}_{1-x}\text{N}$ coatings. In G. Kneringer, P. Rödhammer, and H. Wildner, editors, *16th Int. Plansee Seminar*, volume 2, pages 932–945, Reutte (A), 2005.
- [12] P.H. Mayrhofer, H. Willmann, and A.E. Reiter. Structure and phase evolution of Cr-Al-N coatings during annealing. *Surface and Coatings Technology*, 202(20):4935 – 4938, 2008.
- [13] M. Kawate, A.K. Hashimoto, and T. Suzuki. Oxidation resistance of $\text{Cr}_{1-x}\text{Al}_x\text{N}$ and $\text{Ti}_{1-x}\text{Al}_x\text{N}$ films. *Surface and Coatings Technology*, 165(2):163 – 167, 2003.
- [14] F. Rovere, P.H. Mayrhofer, A. Reinholdt, J. Mayer, and J.M. Schneider. The effect of yttrium incorporation on the oxidation resistance of Cr-Al-N coatings. *Surface and Coatings Technology*, 202(24):5870 – 5875, 2008.

- [15] J.L. Endrino and V. Derflinger. The influence of alloying elements on the phase stability and mechanical properties of AlCrN coatings. *Surface and Coatings Technology*, 200(1-4):988 – 992, 2005.
- [16] J. Soldán, J. Neidhardt, B. Sartory, R. Kaindl, R. Cerstvý, P.H. Mayrhofer, R. Tessadri, P. Polcik, M. Lechthaler, and C. Mitterer. Structure-property relations of arc-evaporated Al-Cr-Si-N coatings. *Surface and Coatings Technology*, 202(15):3555 – 3562, 2008.
- [17] D. Rafaja, M. Dopita, M. Ružička, V. Klemm, D. Heger, G. Schreiber, and M. Šíma. Microstructure development in Cr-Al-Si-N nanocomposites deposited by cathodic arc evaporation. *Surface and Coatings Technology*, 201(6):2835 – 2843, 2006.
- [18] F. Hofer, P. Warbichler, W. Grogger, and O. Lang. On the application of energy filtering TEM in materials science: I. Precipitates in a Ni/Cr-alloy. *Micron*, 26(5):377 – 390, 1995.
- [19] W.C. Oliver and G.M. Pharr. Improved technique for determining hardness and elastic modulus using load and displacement sensing indentation experiments. *Journal of Materials Research*, 7(6):1564–1580, 1992.
- [20] P.H. Mayrhofer and C. Mitterer. High-temperature properties of nanocomposite TiB_xN_y and TiB_xC_y coatings. *Surface and Coatings Technology*, 133-134:131–137, 2000.
- [21] J. Neidhardt, M. O’Sullivan, A.E. Reiter, W. Rechberger, W. Grogger, and C. Mitterer. Structure-property-performance relations of high-rate reactive arc-evaporated Ti-B-N nanocomposite coatings. *Surface and Coatings Technology*, 201(6):2553 – 2559, 2006.
- [22] R. Franz, J. Neidhardt, B. Sartory, R. Tessadri, and C. Mitterer. Micro- and bonding structure of arc-evaporated AlCrVN hard coatings. *Thin Solid Films*, 516(18):6151 – 6157, 2008.
- [23] I. Bertóti. Characterization of nitride coatings by XPS. *Surface and Coatings Technology*, 151-152:194 – 203, 2002.
- [24] X. Wang, W.T. Zheng, H.W. Tian, S.S. Yu, W. Xu, S.H. Meng, X.D. He, J.C. Han, C.Q. Sun, and B.K. Tay. Growth, structural, and magnetic properties of iron nitride thin films deposited by dc magnetron sputtering. *Applied Surface Science*, 220(1-4):30 – 39, 2003.
- [25] G. Soto, W. de la Cruz, and M.H. Fariás. XPS, AES, and EELS characterization of nitrogen-containing thin films. *Journal of Electron Spectroscopy and Related Phenomena*, 135(1):27 – 39, 2004.
- [26] D. Briggs and M. P. Seah, editors. *Practical surface analysis*, volume 1: Auger and X-Ray Photoelectron Spectroscopy. J. Wiley & Sons, Chichester, second edition, 1994.
- [27] C.D. Wagner, W.M. Riggs, L.E. Davis, and J.F. Moulder. *Handbook of X-Ray Photoelectron Spectroscopy*. Perkin-Elmer Corporation, Eden Prairie, Minnesota, 1979.
- [28] D. Brion. Etude par spectroscopie de photoelectrons de la degradation superficielle de FeS_2 , $CuFeS_2$, ZnS et PbS a l’air et dans l’eau. *Applications of Surface Science*, 5(2):133 – 152, 1980 (in French).

-
- [29] V. Di Castro and S. Ciampi. XPS study of the growth and reactivity of FeMnO thin films. *Surface Science*, 331-333, Part A:294 – 299, 1995.
- [30] S. Hüfner. Unfilled inner shells: Transition metals and compounds. In L. Ley and M. Cardona, editors, *Photoemission in Solids II*, volume 27 of *Topics in Applied Physics*, pages 173–216. Springer Berlin/Heidelberg, 1979.
- [31] International Center for Diffraction Data. PDF-2/Release 2007, Card No.: 03-065-2899.
- [32] International Center for Diffraction Data. PDF-2/Release 2007, Card No.: 03-065-0841.
- [33] T.H. de Keijser, J.I. Langford, E.J. Mittemeijer, and A.B.P. Vogels. Use of the Voigt function in a single-line method for the analysis of X-ray diffraction line broadening. *Journal of Applied Crystallography*, 15(3):308–314, 1982.
- [34] J.L. Endrino, G.S. Fox-Rabinovich, and C. Gey. Hard AlTiN, AlCrN PVD coatings for machining of austenitic stainless steel. *Surface and Coatings Technology*, 200(24):6840 – 6845, 2006.
- [35] International Center for Diffraction Data. PDF-2/Release 2007, Card No.: 00-038-1479.
- [36] R.T. Downs. The RRUFF Project: an integrated study of the chemistry, crystallography, Raman and infrared spectroscopy of minerals. Program and Abstracts of the 19th General Meeting of the International Mineralogical Association in Kobe, Japan, 2006.
- [37] J.C. Slater. Atomic radii in crystals. *Journal of Chemical Physics*, 41(10):3199–3205, 1964.
- [38] A. Muan and S. Sōmiya. *Journal of the American Ceramic Society*, 43(4):207, 1960.
- [39] A. Muan and C.L. Lee. *Journal of the American Ceramic Society*, 39(6):207, 1956.

3 Outlook

The results of the present study clearly show the outline for further research on the influence of Fe impurities in AlCrN coatings. To thoroughly investigate the changes in oxidation behaviour with increasing Fe content, a detailed SEM/TEM study should be performed to evaluate the evolution of the oxide layer and confirm the existence of a dense Cr₂O₃-rich surface layer. In this case alternative substrate materials to the used Si have to be considered for annealing experiments at temperatures >1000 °C. The choices are somewhat limited because a good adhesion of the film has to be ensured, while the interdiffusion must be restricted. Currently depositions on MgO and Al₂O₃ substrates show promising results. Furthermore, another deposition series with targets containing 5 at.% of Fe is under way to investigate if the findings presented within the precedent manuscript can also be applied to comparatively high Fe contents.

A detailed characterisation of the influence on the arc evaporation process itself may also prove interesting. In the present study the erosion rate of the targets was determined to be 5-6 g/hour without a correlation with the Fe content. The surface of the targets after deposition was examined by stereomicroscopy but again no change with increasing Fe content could be observed. More information will be obtained by cross sections of the targets, which will be prepared when the further deposition series are completed. Recording of the deposition process with a high speed camera may reveal changes in the cathode spot motion if Fe is present in the targets and round off the research.